

Parallel MRI at ultra-low fields

Vadim S. Zotev ^{a,*}, Petr L. Volegov ^a, Andrei N. Matlashov ^a, Michelle A. Espy ^a,
John C. Mosher ^a, Robert H. Kraus, Jr ^a

^a Los Alamos National Laboratory, Group of Applied Modern Physics, MS D454, Los Alamos, NM 87545, USA

Abstract

Parallel imaging techniques have been widely used in high-field magnetic resonance imaging (MRI). Multiple receiver coils have been shown to improve image quality and allow accelerated image acquisition. Magnetic resonance imaging at ultra-low fields (ULF MRI) is a new imaging approach that uses SQUID (superconducting quantum interference device) sensors to measure the spatially encoded precession of pre-polarized nuclear spin populations at microtesla-range measurement fields. In this work, parallel imaging at ultra-low fields is demonstrated and studied for the first time. A seven-channel SQUID system, designed for both ULF MRI and magnetoencephalography (MEG), is used to acquire 3D images of a human hand and of a preserved sheep brain, as well as 2D images of a large water phantom. The imaging is performed at 46 microtesla measurement field with pre-polarization at 40 mT. It is shown how the use of seven channels increases imaging field of view and improves signal-to-noise ratio for the hand and brain images. Accelerated imaging based on one-dimensional undersampling and 1D SENSE (sensitivity encoding) image reconstruction is studied in the case of the 2D phantom. Actual 3-fold imaging acceleration in comparison to single-shot fully encoded Fourier imaging is demonstrated. These results show that parallel imaging methods are efficient in ULF MRI, and that imaging performance of SQUID-based instruments improves substantially as the number of channels is increased.

Keywords: Parallel MRI, ULF MRI, SENSE, MEG, SQUID

1. Introduction

Parallel magnetic resonance imaging (parallel MRI) is based on simultaneous acquisition of magnetic resonance signals with multiple receiver coils, characterized by distinct spatial sensitivities. Imaging with a coil array generally offers several advantages. First, additional coils enlarge imaging field of view (FOV) by providing sensitivity in those regions where sensitivity of a single coil is low. Second, multiple coils yield higher imaging signal-to-noise ratio (SNR), because MRI signal from each voxel is acquired simultaneously by several coils. The combination of images from the individual coils may improve image quality substantially, especially if it takes into account sensitivity and noise properties of the coils. Third, an array of coils allows accelerated imaging, because the spatial encoding effect of multiple coils is independent of the gradient encoding mechanism of conventional Fourier MRI. This effect can be used to perform some portion of encoding normally done with the gradients, and thus reduce imaging time.

Parallel MRI had been used primarily for FOV and SNR improvement (see, e.g., [1-4]) until about ten years ago, when the focus of parallel imaging studies began to shift

towards imaging acceleration. This transition was precipitated by the progress in MRI technology and the need for faster medical imaging. Accelerated image acquisition in parallel MRI is achieved at the expense of reduction in imaging SNR. It is usually realized by undersampling along the phase encoding direction(s) that would lead to reduced FOV and aliasing in conventional Fourier imaging. Parallel MRI reconstruction methods incorporate coil spatial sensitivities to generate full-FOV images without aliasing from the undersampled data acquired with multiple channels. These methods can be divided into k -space (such as SMASH [5]), image-domain (SENSE [6]), and hybrid (such as non-Cartesian SENSE [7]) approaches. They can be formulated and compared within the same theoretical framework [8,9]. Parallel imaging methods are essential in MRI applications requiring high temporal resolution, such as cardiovascular MRI [10], abdominal MRI [11], and functional MRI of the human brain [12]. Acceleration factors as high as 16 have been reported [11], though 2- or 3-fold accelerations are typical in clinical practice. Yet higher temporal resolution can be achieved if parallel imaging is combined with magnetic source localization by a large sensor array [13] used in magnetoencephalography (MEG) [14].

Parallel imaging methods have to date only been applied in high-field MRI with measurement fields of ≥ 1.5 T. Magnetic resonance imaging at ultra-low fields (ULF MRI)

* Corresponding author. Fax: +1 505 665 4507.

E-mail address: vzotev@lanl.gov (V.S. Zotev).

is a new imaging approach that uses measurement fields in the microtesla range [15-24]. Efficiency of MRI is ultimately limited by the broadening of the NMR signal linewidth, which is determined by absolute inhomogeneity of the magnetic field. For a fixed relative inhomogeneity, the absolute field inhomogeneity scales linearly with the field strength [15]. Because of this, ultra-low fields of modest relative homogeneity are highly homogeneous on the absolute scale, and very narrow NMR lines with high SNR are achieved [15,19,23]. This fact greatly simplifies coil design and makes it possible to construct ULF MRI systems that are simple, inexpensive, portable, and patient-friendly. Imaging at ULF offers additional benefits, including minimized susceptibility artifacts [15], enhanced T_1 contrast [25], and possibility of imaging in the presence of metal [19,26]. Moreover, ULF MRI is compatible with magnetoencephalography as discussed below.

Implementation of MRI at ultra-low fields encounters two problems: insufficient magnetization of a sample by microtesla fields, and low efficiency of Faraday detection at kilohertz-range frequencies. The first difficulty is typically resolved by using the pre-polarization technique [27]. In this approach, the sample is pre-polarized by a relatively strong (up to 100 mT and higher) magnetic field prior to each imaging step. The second problem can be solved by measuring NMR signals with highly sensitive SQUID (superconducting quantum interference device) sensors [28-31]. SQUIDs with untuned input circuit are typically employed [15-24], because their response is independent of frequency. Low-field images acquired using tuned SQUID pre-amplifiers [29], as well as Faraday detector coils [32,33], have also been reported, though the method of [15-24] appears to be more efficient. Despite these improvements, insufficiently high SNR remains a major limitation in present-day ULF MRI. The SNR can be improved by stronger pre-polarization, which makes the situation similar to that in conventional MRI with its quest for higher magnetic fields. The pre-polarizing field in ULF MRI, however, does not need to be very uniform, because no spin precession is measured during the pre-polarization.

One property of ULF MRI makes it particularly attractive: it can be easily combined with SQUID-based techniques for biomagnetic measurements, such as magnetoencephalography (MEG) [14] and magneto-cardiography (MCG) [34]. It has been demonstrated that ULF NMR signals, generated inside a human body, can be measured simultaneously with MEG [20] or MCG [21] signals using the same SQUID sensor. A seven-channel SQUID system has been used by the authors to acquire ULF MRI images of a human hand and perform auditory MEG [22]. Combination of MEG and ULF MRI capabilities in a multi-channel whole-head SQUID system will eliminate the need for MEG/MRI co-registration and may allow simultaneous functional (MEG) and anatomical (ULF MRI) imaging of the human brain. Because MEG instruments include large arrays (typically hundreds) of

SQUID sensors, parallel imaging techniques should be very efficient in ULF MRI. Similar to conventional high-field imaging, multiple sensors can be used at ultra-low fields to improve imaging FOV, SNR, and speed. Image distortions due to concomitant gradients, however, are more pronounced at ULF, and need to be corrected as FOV increases [35-37].

In this work, the first study of parallel MRI at ultra-low fields is reported. The new seven-channel SQUID system [22], specially designed for both ULF MRI and MEG, is used to acquire 3D images of a human hand and of a preserved sheep brain, as well as 2D images of a large phantom. Improvements in imaging FOV and SNR by the sensor array are demonstrated in the case of the hand and brain images. Actual 3-fold imaging acceleration is achieved in the phantom experiment using SENSE (sensitivity encoding) method [6].

2. Materials and methods

2.1 Instrumentation

All experimental results, reported in this paper, were obtained using a seven-channel SQUID system for 3D ULF MRI and MEG, depicted schematically in Fig. 1. The system was initially used to acquire 2D images of a human hand and perform auditory MEG measurements [22]. It has been subsequently modified for 3D imaging, as described here briefly. The system includes seven second-order SQUID gradiometers with 37 mm diameter and 60 mm baseline, characterized by magnetic field resolutions of $1.2\ldots2.8 \text{ fT}/\sqrt{\text{Hz}}$ at 1 kHz [22]. The gradiometers are installed parallel to one another inside a flat-bottom liquid helium cryostat. Their pick-up coils form a symmetric pattern shown in Fig. 1A with 45 mm center-to-center spacing of the neighboring coils. Each SQUID sensor is equipped with a cryoswitch [22] that protects it from transients caused by switching fields and gradients in ULF MRI experiments. All measurements are performed inside a magnetically shielded room.

As mentioned in the introduction, the measurement field and encoding gradients for ULF MRI can be generated by simple and inexpensive coil systems. Schematic of our coil system is shown in Fig. 1B. The ultra-low measurement field B_m is created along the Z axis by a pair of round Helmholtz coils, 120 cm in diameter. The strength of the B_m field is approximately 46 μT , which corresponds to proton Larmor frequency of about 1940 Hz. Three sets of coils generate three gradients for 3D Fourier imaging. The longitudinal gradient $G_z=dB_z/dz$ is produced by a pair of square Maxwell coils, orthogonal to the Z axis. A specially designed set of eight rectangular coils orthogonal to the X axis provides the transverse gradient $G_x=dB_x/dx$. The second transverse gradient, $G_y=dB_y/dy$, is generated by a set of four rectangular coils orthogonal to the Y axis.

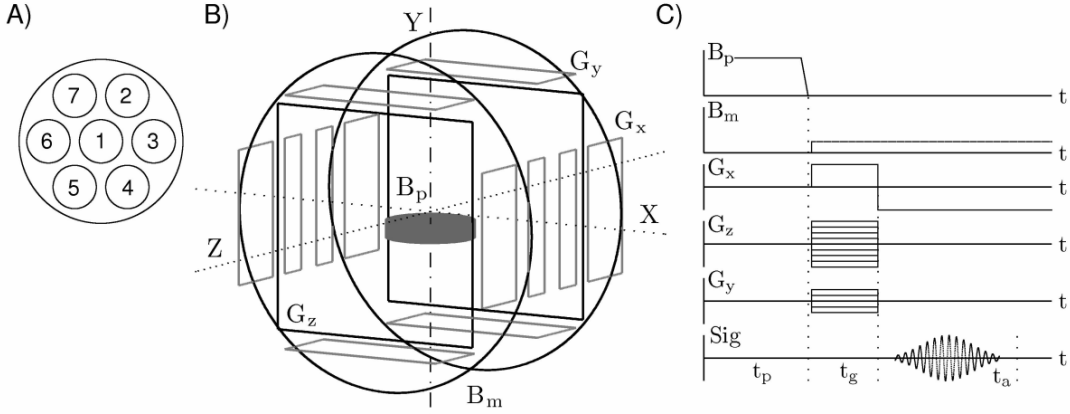


Fig. 1. The seven-channel system for 3D ULF MRI and MEG. (A) Positions of the SQUID channels inside the cryostat, (B) schematic of the coil system, (C) 3D Fourier imaging sequence with pre-polarization and gradient echo.

The pre-polarizing field B_p in the present system is three orders of magnitude stronger than the measurement field B_m . It is produced by a massive cylindrical coil positioned below the sample space and immersed in a liquid nitrogen bath. The vertical component of the B_p field varies between 40 and 50 mT at 28 A current across the sample space.

The 3D imaging procedure, used in our experiments, is shown in Fig. 1C. Each imaging step begins with pre-polarization of a sample by the field B_p during time t_p . The pre-polarizing field is then turned off rapidly, and the measurement field B_m is applied. In the present set-up, the B_p field is ramped down linearly in 6 ms, and the B_m field is applied 3-4 ms later, by which time all transients, induced by the B_p pulse in the system coils, are dissipated. The application of the measurement field B_m perpendicular to the original direction of B_p induces spin precession. Imaging is then performed according to the standard 3D Fourier imaging protocol with gradient echo. Spin precession is phase encoded by two gradients, G_z and G_y , during time t_g , and gradient echo is created by reversal of the frequency encoding gradient G_x . The echo signal is measured during the acquisition time t_a with discrete sampling at 16 kHz. The sequence in Fig. 1C is repeated for all combinations of the selected G_z and G_y values, and a 3D image is reconstructed from the acquired data by 3D fast Fourier transform.

2.2 Imaging parameters

The seven-channel system depicted in Fig. 1 was used to perform ULF MRI of objects shown in Fig. 2. They include a human hand, a sheep brain, preserved in formaldehyde, and a water phantom. Imaging of the sheep brain was performed as a preparatory step for human brain imaging. The phantom was constructed using a polyethylene disc with flat-bottom holes (19 mm in diameter and 19 mm deep) drilled in the pattern

shown (Fig. 2) with 22 mm center-to-center spacing. The holes were filled with tap water with experimentally determined transverse relaxation time $T_2^* \approx 2.8$ s. The mean relaxation time T_2 for the human hand was measured to be ≈ 120 ms. For the preserved sheep brain, this time was only $T_2 \approx 40$ ms. For comparison, T_2 time of a living human brain is 80-100 ms (at high fields).

In the human hand experiment, the following imaging parameters were used (Fig. 1C). The hand was pre-polarized for $t_p=0.5$ s. The gradient encoding and signal acquisition times were $t_g=42$ ms and $t_a=84$ ms, respectively. The frequency encoding gradient G_x changed between ± 94 μ T/m (± 40 Hz/cm). The phase encoding gradient G_z had $N_z=55$ different values, that were equally spaced and symmetric with respect to $G_z=0$, with the maximum value $G_{z,max} = -G_{z,min} = 94$ μ T/m (40 Hz/cm). Similarly, $N_y=9$ values were selected for the gradient G_y , with the maximum value $G_{y,max} = -G_{y,min} = 47$ μ T/m (20 Hz/cm). These imaging parameters provided 3 mm \times 3 mm \times 6 mm resolution, with the 6 mm pixel size corresponding to the vertical dimension. A single scan of k space included 495 measurements and required 5 min. To improve image quality, results of 12 consecutive scans were averaged. The total imaging time was about one hour. It should be noted, however, that 80% of this time was taken up by pre-polarization.

The imaging procedure in the sheep brain experiment was similar to the one used for the human hand. Because of the short T_2^* , however, the encoding and acquisition times were chosen to be shorter, and the gradients – stronger. The imaging parameters in this case had the following values: $t_p=0.5$ s, $t_g=33$ ms, $t_a=66$ ms, $G_x = \pm 140$ μ T/m (± 60 Hz/cm), $N_z=33$, $G_{z,max} = -G_{z,min} = 140$ μ T/m (60 Hz/cm), $N_y=11$, $G_{y,max} = -G_{y,min} = 70$ μ T/m (30 Hz/cm). The imaging resolution was 2.5 mm \times 2.5 mm \times 5 mm. One scan took about 4 min.



Fig. 2. Objects for imaging: a human hand, a preserved sheep brain, and a water phantom.

Because the echo time in this experiment (≈ 70 ms after the application of B_m) was longer than $T_2^* \approx 40$ ms, magnitude of the measured signal was substantially reduced by the transverse relaxation. To improve image quality for deep-lying layers of the sheep brain, 42 scans were performed, and their results averaged. The entire experiment took about 3 hours. We expect ULF imaging of a living human brain to be faster because of the longer T_2 time in that case.

The purpose of the 2D water phantom experiment was to demonstrate imaging acceleration by using parallel image reconstruction. Parameters of the imaging procedure, therefore, were selected to maximize SNR and allow single-shot acquisition (without signal averaging). They had the following values: $t_p=4$ s, $t_g=250$ ms, $t_a=500$ ms, $G_x= \pm 23.5$ $\mu\text{T}/\text{m}$ (± 10 Hz/cm), $N_z=73$, $G_{z,\text{max}} = -G_{z,\text{min}} = 23.5$ $\mu\text{T}/\text{m}$ (10 Hz/cm), $N_y=1$, $G_y=0$. This 2D imaging sequence provided 2 mm \times 2 mm resolution in the XZ plane. Because of the long pre-polarization time required to polarize water, single-shot acquisition of a full-FOV phantom image took about 6 min.

After each of the three imaging experiments, sensitivity maps of the seven channels were acquired by imaging a large uniform water phantom placed under the cryostat instead of the studied object. The imaging resolution was the same as in the main experiment. The imaging parameters were also the same except for smaller increment value and greater number of steps N_z for the G_z gradient to obtain a larger FOV in the Z direction. The pre-polarization time for the uniform water phantom was at least 2 s.

2.3 Concomitant gradient correction

The system of seven pick-up coils, shown in Fig. 1A, provides the imaging FOV in the horizontal XZ plane that is approximately 3 times as wide as the FOV of a single coil. Because image distortions caused by concomitant gradients grow quadratically with the distance from the imaging center, they become more pronounced as FOV increases. While correction of concomitant gradient artifacts is rather complicated in

the general case [35,36], it can be simplified for the imaging parameters used in our experiments.

It has been shown [37] that image distortions due to concomitant gradients can be characterized by a dimensionless parameter $\varepsilon=L(G/B_m)$, where L is the object size, G is the imaging gradient strength, and B_m is the measurement field. The ratio B_m/G is a curvature radius that describes how straight lines within the object become curved in the MRI image. In our human hand experiment, $L_z \approx L_x \approx 14$ cm and $L_y \approx 4$ cm. The parameter ε for the G_y gradient, $L_y(G_{y,\text{max}}/B_m)=0.04$, is thus seven times lower than for the G_z gradient, $L_z(G_{z,\text{max}}/B_m)=0.29$. Because the concomitant gradient artifacts associated with G_z (and G_x) are rather small, as shown below, the effect of G_y can be safely neglected. It is sufficient, therefore, to consider a two-dimensional problem in the XZ plane.

Following the analysis of [36], we can write for the gradient echo sequence with G_x and G_z gradients:

$$x_{\text{MRI}} \approx x + \frac{G_x}{2B_m} z^2, \quad (1)$$

$$z_{\text{MRI}} \approx \left(1 + \frac{G_x}{2B_m} x\right) \cdot z + \frac{G_z}{8B_m} x^2. \quad (2)$$

In these formulas, (x, z) are coordinates of a voxel inside an object, $(x_{\text{MRI}}, z_{\text{MRI}})$ are coordinates of the corresponding pixel in the MRI image, G_x is the readout gradient (after the reversal), and G_z is a given value of the phase encoding gradient. Eq. (1) and the first term in Eq. (2) depend on the constant G_x , and describe geometrical deformation of the image. The last term in Eq. (2) depends on the gradient G_z that takes a discrete set of values and causes blurring of the image along the Z direction [36]. In the human hand experiment, the ratio $G_x/2B_m$ is equal to $-1.03 \cdot 10^{-2}$ cm^{-1} . For the maximum value of $|z| \approx 7$ cm, the difference $x_{\text{MRI}} - x$ is about -5 mm. The last term in Eq. (2) is four times smaller even for the largest $G_{z,\text{max}}=|G_x|$ and $|x| \approx 7$ cm, and equals 1.25 mm in that case. Therefore, the magnitude of image blurring in the worst case is less than the pixel size (3 mm). The same applies to the sheep brain experiment. Based on these estimates, we

neglect the last term of Eq. (2) in the present work.

The effect of concomitant gradients can then be described as a deformation of an image that makes lines of constant x curved, and lines of constant z – tilted. As a result, the Fourier reconstructed image becomes pointed (i.e. convex and narrowing) in the direction of decreasing readout frequencies. The corrected image can be obtained by transformation of coordinates $(x_{\text{MRI}}, z_{\text{MRI}})$ to (x, z) according to Eq. (1) and Eq. (2) (without the last term). Results of such correction are presented in Sections 3.1 and 3.2.

2.4 SENSE image reconstruction

Accelerated image acquisition in the phantom experiment was achieved by undersampling along the phase encoding direction Z . Non-aliased full-FOV images were then reconstructed using SENSE method [6]. In the simplest case of 2D Fourier imaging, this method (1D SENSE) works as follows.

The number of phase encoding steps, and thus the scan time, is reduced by factor R , called the reduction (or acceleration) factor. This is accomplished by increasing the increment value for the phase encoding gradient G_z while preserving its limiting values. The spatial resolution remains unchanged, but the imaging FOV along the phase encoding direction is reduced by the factor R , which causes aliasing. This means that the image signal at an aliased pixel within the reduced FOV is a superposition of up to R signals corresponding to equidistant pixels in the full FOV. The SENSE image reconstruction from the undersampled data is performed in two steps. First, reduced-FOV aliased images from individual detector coils are obtained via discrete Fourier transform. Second, a non-aliased full-FOV image is reconstructed from the individual images using full-FOV sensitivity maps for all the coils. Because different coils in an array have different local sensitivities, the superposition of R signals due to aliasing occurs with different weights for different coils [6], and can be undone by means of linear algebra if the number of coils is greater than R . This allows unfolding of the aliased images.

The imaging acceleration, however, is achieved at the expense of reduction in signal-to-noise ratio. The SNR at a given pixel after SENSE reconstruction with a certain R is related to the SNR at the same pixel in a fully encoded image as $\text{SNR}_R = \text{SNR}_F / (g\sqrt{R})$, according to [6]. The factor \sqrt{R} in the denominator results from the R -fold overall reduction in the acquisition time. The factor $g \geq 1$, called the geometry factor, describes local noise amplification in the unfolded image. It depends on both R and geometry of the sensor array. Section 3.3 presents SENSE reconstructed images of the 2D phantom and corresponding g factor maps for different values of R .

3. Results

In this Section, we experimentally demonstrate the benefits of using multiple channels in ULF MRI. The FOV improvement is studied in the case of the human hand, because of its large size. Images of the preserved sheep brain are used to demonstrate the increase in SNR. Because this brain is small enough to be imaged by a single channel, a meaningful comparison of single-channel and multi-channel images is possible. The imaging acceleration is studied for the 2D water phantom, because SNR in this case is sufficiently high and allows imaging without signal averaging.

3.1 Demonstration of FOV improvement

Results of 3D imaging of a human hand at 46 μT measurement field are exhibited in Fig. 3. The experiment was performed as described in Section 2.2. Each image in Fig. 3 represents a 6 mm thick horizontal layer of the hand with the vertical position of that layer's central plane specified by coordinate Y . The imaging resolution in the XZ plane is 3 mm \times 3 mm. The coordinates are given with respect to the center of the imaging coil system. The bottom of the cryostat is located at $Y \approx 25$ mm. Each image in Fig. 3 is a composite seven-channel image, computed as a square root of the sum of squares of images from the seven individual channels with the same Y . The composite images were subjected to fine-mesh bicubic interpolation, followed by correction of concomitant gradient artifacts as explained below. The images in Fig. 3 are proton density images with some T_2 contrast (because measurement starts about 50 ms after B_m is applied). They show important anatomical features of the hand, including soft tissues, joints, and bones.

Fig. 4 shows seven individual-channel images of the layer with $Y=12$ mm. The images are exhibited with different intensity scales to emphasize the extent of each channel's FOV. According to Fig. 4, any single channel in our system can only image a part of the hand. The array of seven channels used simultaneously, however, expands the FOV and allows high quality imaging of the whole hand.

Image distortions caused by concomitant gradients are studied in Fig. 5. This figure exhibits a sensitivity map and a 2D hand image both before (A) and after (B) the concomitant gradient correction. 3D sensitivity maps were obtained for all the channels by imaging a large and thick uniform water phantom. The map in Fig. 5 is a composite seven-channel sensitivity map for $Y=18$ mm, corresponding to the top image layer in Fig. 3. The 2D hand image was computed from the 3D data as a square root of the sum of squares, with summation over seven channels and four image layers. The ratio $G_x/2B_m$ in Eqs. (1) and (2) is equal to $-1.03 \cdot 10^{-2} \text{ cm}^{-1}$ in this experiment. According to Fig. 5, the sensitivity

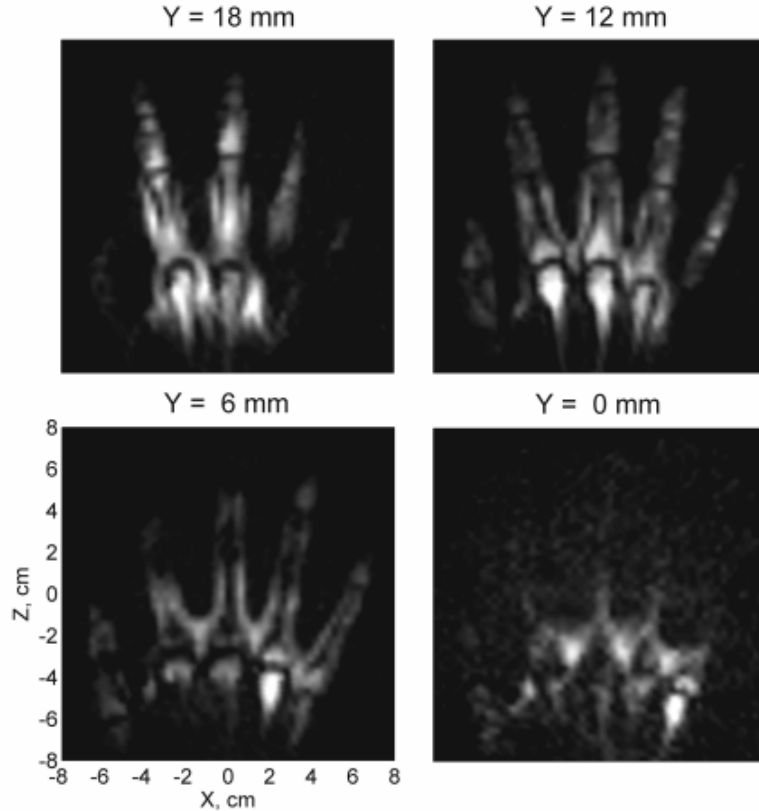


Fig. 3. Composite seven-channel 3D image of the human hand acquired at $46 \mu\text{T}$.

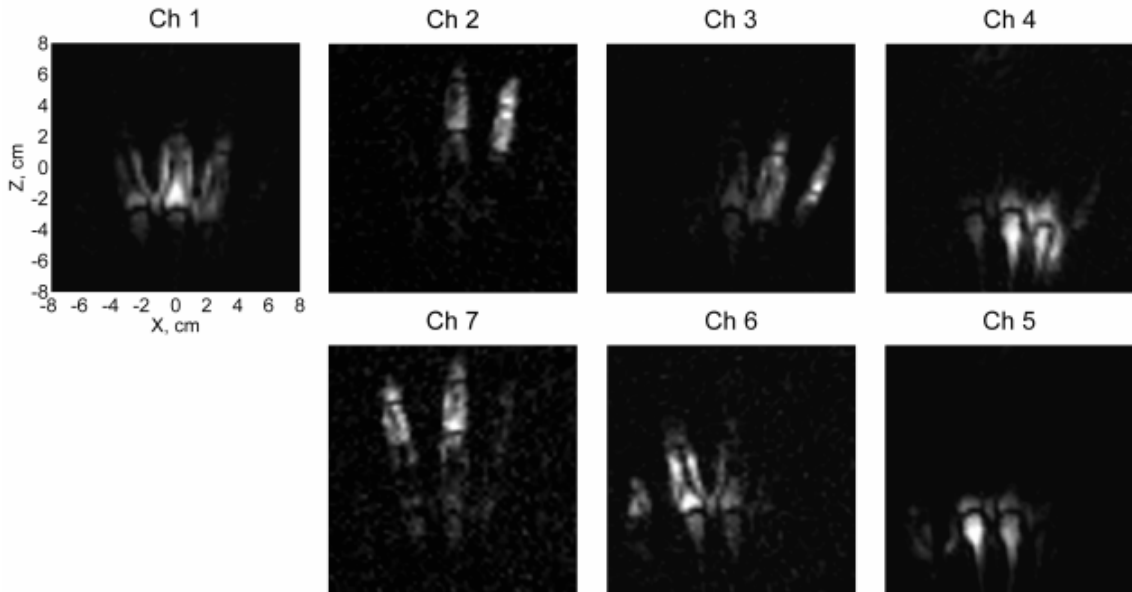


Fig. 4. Images from the seven individual channels for $Y=12 \text{ mm}$.

map before the correction (A) is visibly deformed: it is convex to the right and narrows from the left to the right. This is the direction (from Ch 6 to Ch 3) in which the readout frequency decreases. The hand image (A) exhibits similar distortion.

Correction of concomitant gradient artifacts is performed in two steps. First, the size of the image element is reduced by fine-mesh bicubic interpolation. Then, the image coordinates are transformed from $(x_{\text{MRI}}, z_{\text{MRI}})$ to (x, z) according to Eq. (1) and Eq. (2)

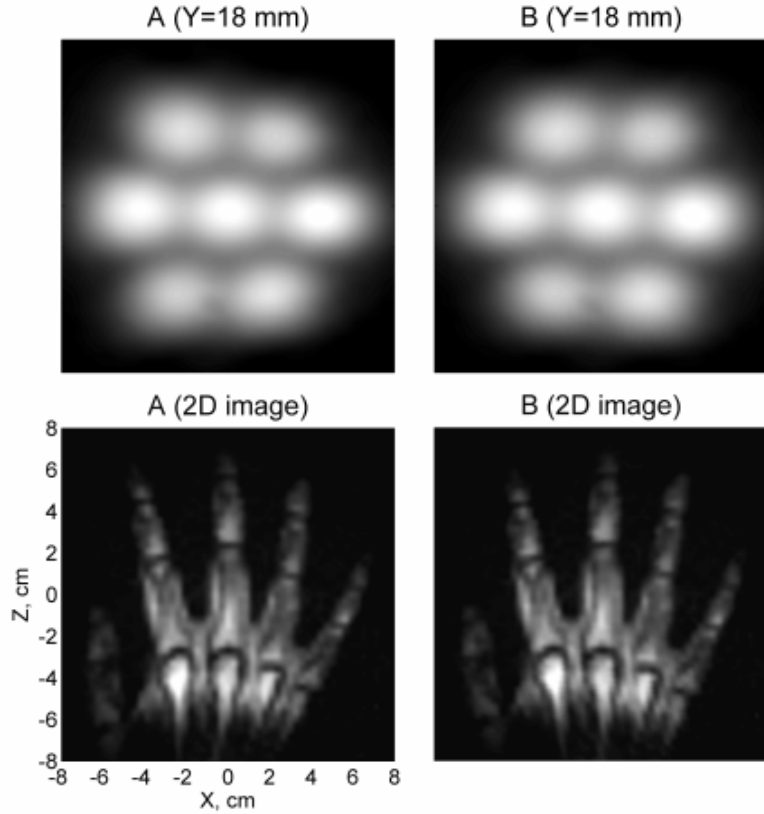


Fig. 5. Images before (A) and after (B) correction of concomitant gradient artifacts.

(without the last term). Fig. 5 shows that the sensitivity map becomes more symmetric after such correction (B). It should be noted that the whole sensitivity map is slightly turned clockwise with respect to the X axis because of the imperfect orientation of the cryostat. The corrected image of the hand (B) features straight fingers, and more closely resembles the photograph in Fig. 2. These results show that geometrical image distortions caused by concomitant gradients are relatively small in our experiments, and can be easily corrected in the final images.

3.2 Demonstration of SNR improvement

ULF MRI images of the preserved sheep brain are shown in Fig. 6. As in the human hand experiment, imaging of the brain was performed according to the standard 3D Fourier procedure (Fig. 1C) with parameters specified in Section 2.2. Each image in Fig. 6 has $2.5 \text{ mm} \times 2.5 \text{ mm}$ in-plane resolution and corresponds to a 5 mm thick horizontal layer of the brain. The layer's position is given by the Y coordinate of its central plane. The images in Fig. 6 are composite seven-channel images with sensitivity correction. They were computed using the channels' images and sensitivity maps according to the maximum SNR multicoil algorithm [2], which is equivalent to SENSE

method [6] with $R=1$. The images were also subjected to fine-mesh bicubic interpolation and correction of concomitant gradient artifacts. The brain images are T_2 weighted, with darker regions characterized by shorter T_2 times.

Fig. 7 exhibits images of one brain layer with $Y=5$ mm, acquired by the seven individual channels. Different images in Fig. 7 have different intensity scales to make contribution region of each channel clearly visible. In contrast to the human hand experiment (Fig. 4), the entire sheep brain can be imaged by channel 1. Each of the six surrounding channels provides additional information about a certain part of the brain. Because any voxel in the brain is imaged simultaneously by two or more channels, the composite seven-channel image has higher SNR than the image from channel 1 only.

The SNR improvement by the sensor array can be clearly observed in Fig. 8, which compares images acquired by one, six, and seven channels, respectively. Each multi-channel image was computed as a square root of the sum of squares without sensitivity correction. According to Fig. 8, the six channels surrounding channel 1 provide substantial (~ 3 times) signal improvement in the areas near the edges of the brain, where sensitivity of channel 1 is low. The average signal intensity in the composite seven-channel

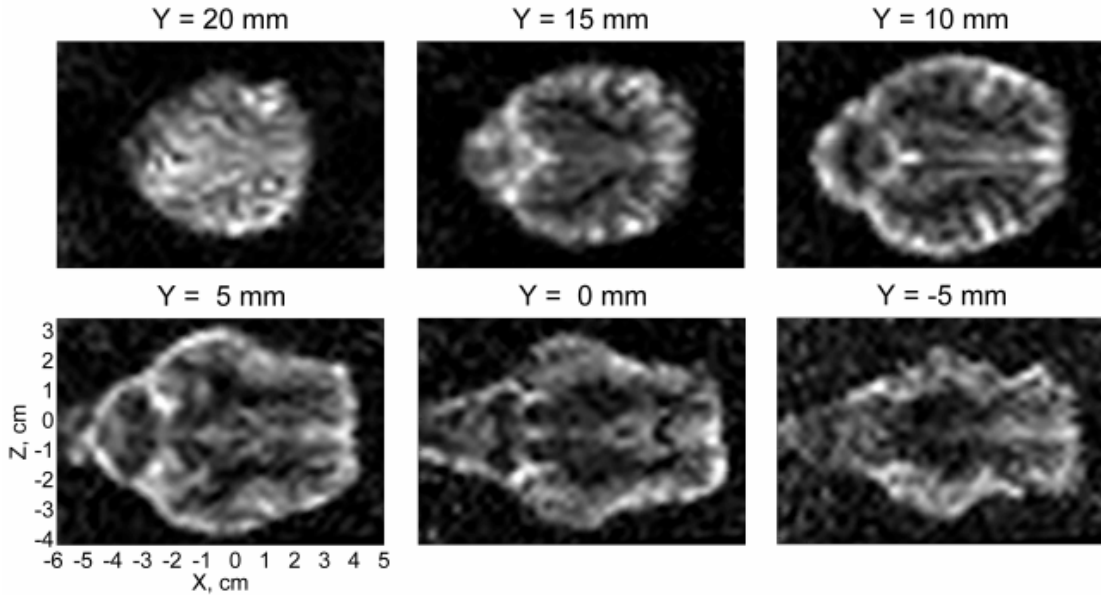


Fig. 6. Composite seven-channel 3D image of the preserved sheep brain acquired at $46 \mu\text{T}$.

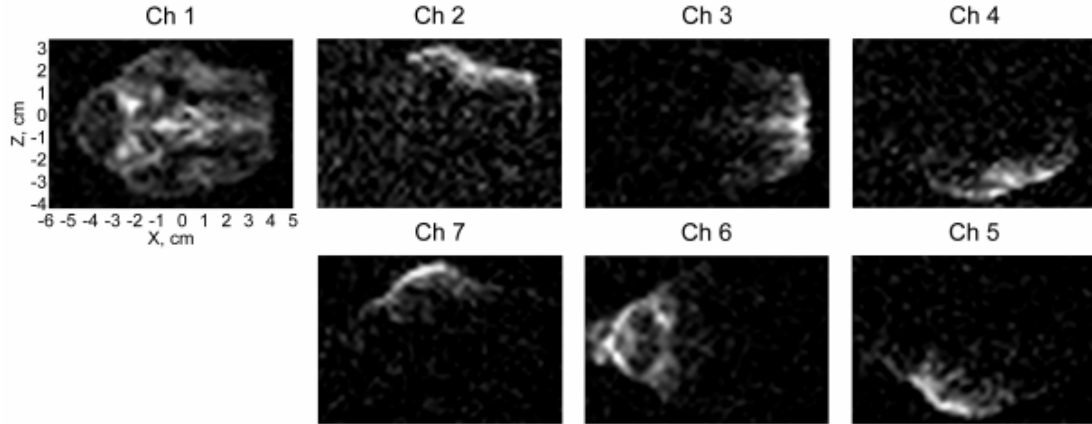


Fig. 7. Images from the seven individual channels for $Y=5 \text{ mm}$.

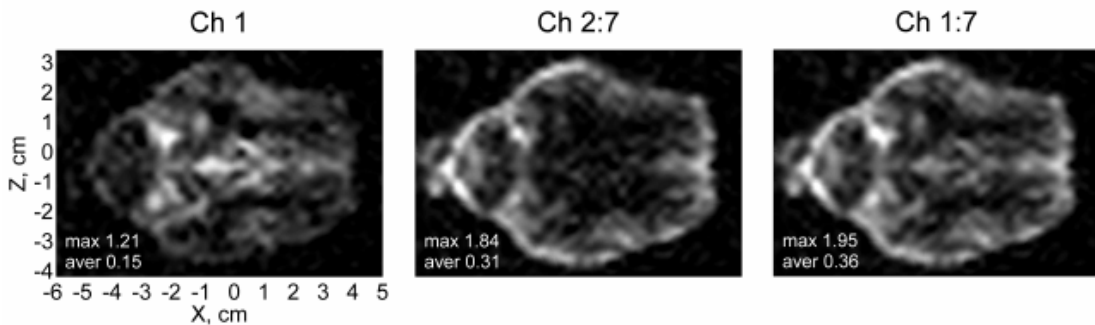


Fig. 8. Comparison of images (with $Y=5 \text{ mm}$) acquired by one, six, and seven channels.

image is 2.4 times higher than in the image acquired by channel 1.

To have a more general and more precise description of FOV and SNR improvement effects, one should compare sensitivity maps rather than object images. Fig. 9 exhibits one layer of a composite seven-channel

3D sensitivity map, acquired by imaging a large uniform water phantom with the same resolution as in the sheep brain images. The map was calculated as a square root of the sum of squares of the individual-channel images with $Y=20 \text{ mm}$. The direction of B_m in the sheep brain experiment was opposite to that in the

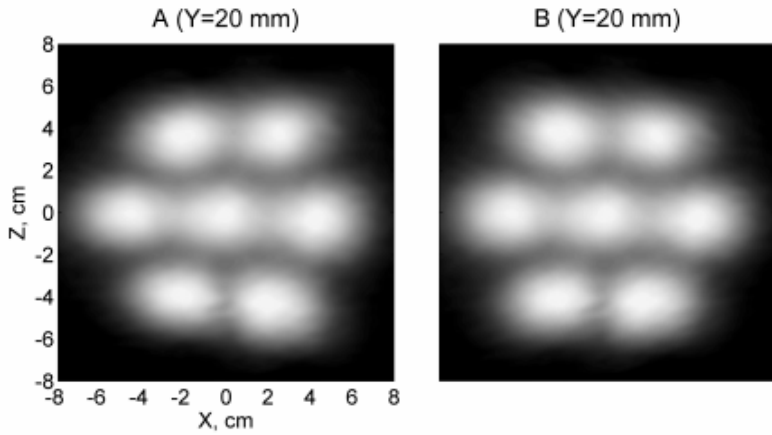


Fig. 9. One layer of 3D sensitivity map before (A) and after (B) concomitant gradient correction.

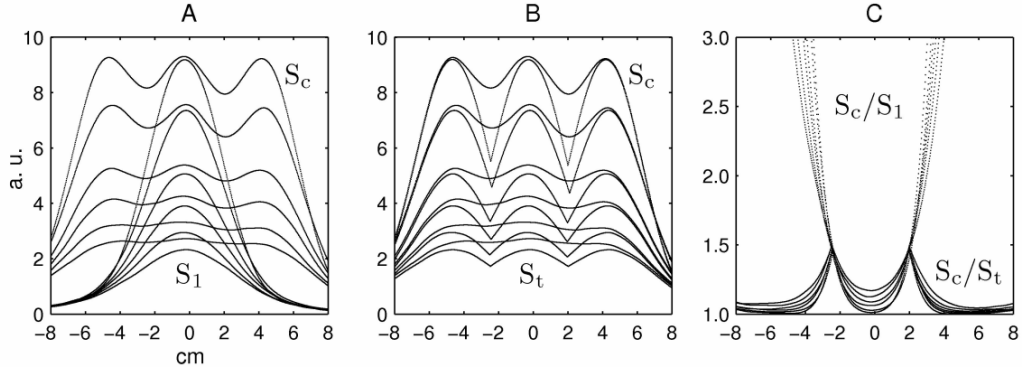


Fig. 10. Sensitivity profiles along the line of channels 1, 3, and 6 for six image layers. S_1 – sensitivity of channel 1, S_c – composite seven-channel sensitivity, S_t – combination of truncated single-channel sensitivities.

human hand measurements. The ratio $G_x/2B_m$ is equal to $+1.55 \cdot 10^{-2} \text{ cm}^{-1}$ in this case. The readout frequency decreases from Ch 3 (on the right) to Ch 6 (on the left). The original sensitivity map in Fig. 9A is deformed and points in the same direction, i.e. to the left. The sensitivity map after the correction of concomitant gradient artifacts according to Eq. (1) and Eq. (2) (without the last term) is shown in Fig. 9B. It is symmetric and similar to the map in Fig. 5B. Because the sheep brain is relatively small in size, the brain images before and after the correction differ only slightly.

Fig. 10 compares multi-channel and single-channel sensitivity maps for different image layers. It shows sensitivity profiles along a straight line that passes through the sensitivity centers of channels 1, 3, and 6 (Fig. 1A). This line is slightly turned with respect to the X axis as seen in Fig. 9B. The sensitivity profiles correspond to six image layers with the same values of Y as in Fig. 6. They were derived from experimental sensitivity maps and digitally smoothed. The single-peak curves (S_1) are sensitivity profiles of channel 1. The smooth curves with three maxima (S_c) represent

composite (square root of the sum of squares) seven-channel sensitivities as the one in Fig. 9B. The curves with sharp dips (S_t) are constructed from truncated sensitivity profiles of channels 1, 3, and 6, so that $S_t = \max[S_1, S_3, S_6]$ at any point.

The ratio S_c/S_1 , plotted in Fig. 10C, describes the overall sensitivity increase when the seven-channel array is used instead of channel 1. While the sensitivity improvement at the center of the system is modest (from 1% for the top to 18% for the bottom layer), it becomes very pronounced (10 times and more) as the observation point moves from the center towards any of the outside channels. This sharp increase in sensitivity, however, results from the FOV expansion: additional channels provide high sensitivity in those areas where sensitivity of channel 1 is low, as can be seen in Fig. 10A. To estimate the SNR improvement due to overlapping sensitivities, the ratio S_c/S_t can be considered. Because S_t coincides with a single-channel sensitivity at any point, S_c/S_t can significantly differ from 1 only in those areas where more than one channel contributes substantially to the composite sensitivity S_c . According to Fig. 10C, the ratio S_c/S_t

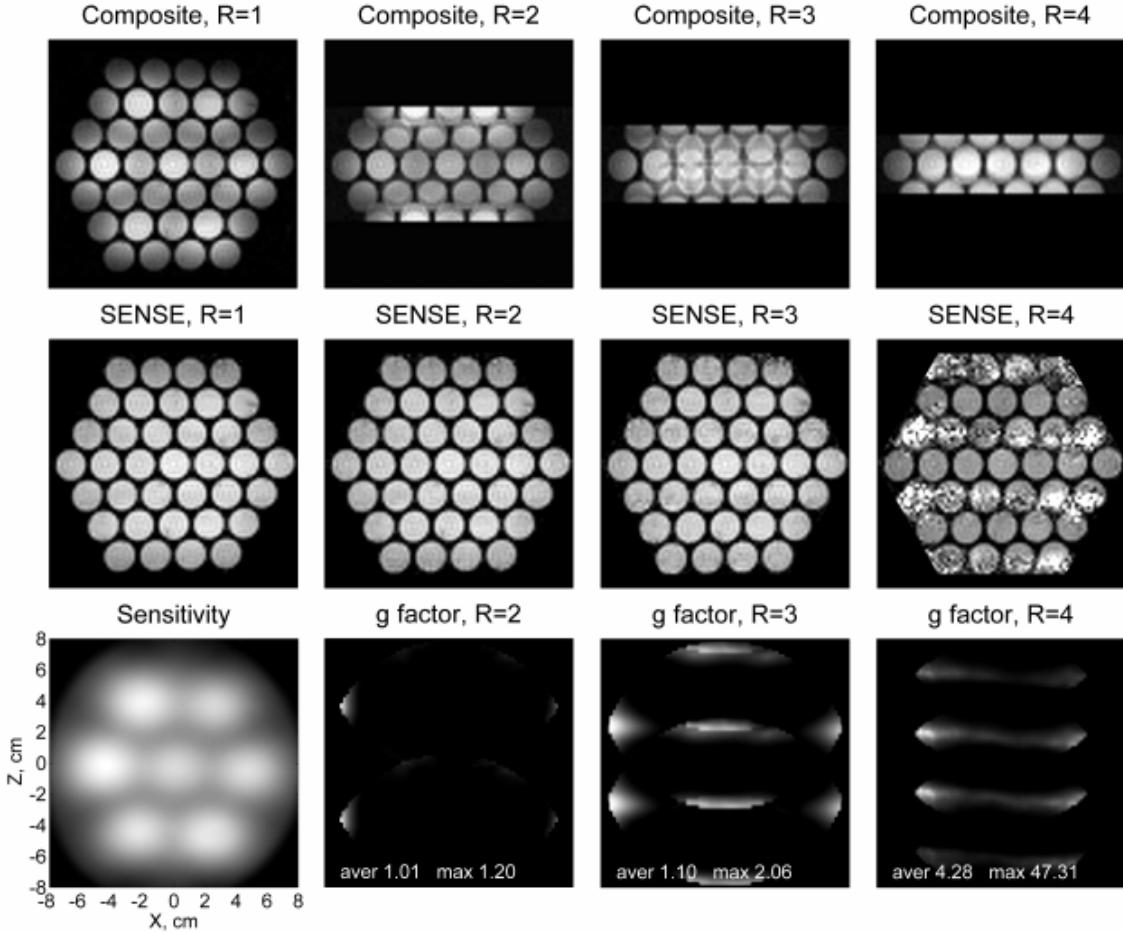


Fig. 11. SENSE reconstruction of 2D phantom images for different values of the acceleration factor R .

reaches its maxima between two channels, where channel sensitivities overlap the most. These maxima have magnitude of about 1.5, which is greater than $\sqrt{2}$, because more than two channels contribute to S_c . Away from the maxima, S_c/S_t is larger for deeper image layers, because channels' sensitivity regions in the horizontal plane become wider with the distance from the pick-up coils. In general, if N channels have equal sensitivities at a given point, their composite (square root of the sum of squares) sensitivity will be \sqrt{N} times higher. Because there can only be three neighboring coils in our array, the SNR improvement due to sensitivity overlaps cannot be much larger than $\sqrt{3}$.

3.3 Demonstration of imaging acceleration

Results of the 2D phantom imaging experiment are presented in Fig. 11. The imaging was performed with $2 \text{ mm} \times 2 \text{ mm}$ resolution according to the procedure described in Section 2.2. Because the imaging gradients were relatively weak in this experiment, no correction of concomitant gradient artifacts was employed. The top row of images in Fig. 11 contains composite (square root of the sum of squares) seven-channel

images acquired with different degrees of undersampling along the phase encoding direction Z characterized by the reduction factor R . Single-shot acquisition of the full-FOV image with $R=1$ included 73 phase encoding steps and required 6 min. For $R>1$, these values were reduced R times, as explained in Section 2.4. The number of phase encoding steps, taken symmetrically with respect to $G_z=0$, was $2[36/R]+1$, and the total imaging time was approximately $6/R$ min. The accelerated image acquisition based on such undersampling led to reduced FOV and aliasing, as seen in the composite images with $R=2,3,4$. The middle row in Fig. 11 exhibits corresponding full-FOV images reconstructed from the undersampled data using 1D SENSE method with experimentally determined sensitivity maps of the sensors. The composite seven-channel 2D sensitivity map is shown as the first image in the bottom row of Fig. 11. The other images in that row are maps of the geometry factor for $R=2,3$, and 4.

According to Fig. 11, the SENSE reconstruction provides nearly perfect phantom images for $R=1, 2$, and 3. In the case of $R=1$, the SENSE method reduces to the maximum-SNR multicoil sensitivity correction [2]

without unfolding. The corrected image shows more uniform intensity distribution than the composite image with $R=1$. The SENSE algorithm allows successful unfolding of the aliased images with $R=2$ and $R=3$, enabling accelerated image acquisition. The SENSE image with $R=4$, however, is marked by excessive noise. This result is consistent with behavior of the geometry factor, that quantitatively describes local noise amplification in the unfolded images. While the maximum g factor values for $R=2$ and $R=3$ are 1.20 and 2.06, respectively, the maximum value for $R=4$ is as high as 47. This means that the SENSE reconstruction becomes increasingly unstable for $R \geq 4$, suggesting that the spatial information provided by the sensor array is no longer sufficient for unfolding the aliased images.

This limitation can be easily understood if one considers the sensitivity map in Fig. 11. Because the pick-up coils in our system form a two-dimensional array and have substantially localized sensitivities, any straight line parallel to the Z axis intersects essential sensitivity regions of at most three coils. Thus, no more than three coils can efficiently participate in 1D SENSE reconstruction for any given set of pixels related by aliasing. As a result, the maximum practical acceleration of $R=3$ is lower than the number of channels in our system. Two-dimensional sensor arrays are known to provide lower acceleration factors in the case of 1D undersampling than one-dimensional arrays with the same number of elements [38]. Higher accelerations can be achieved in 3D Fourier imaging by undersampling along each of the two phase encoding directions and reconstructing images with 2D SENSE [39]. This approach, however, is not very practical with our present system, because it would require phase encoding to be performed along X, and frequency encoding – along Y direction, which is inefficient due to the limited sensitivity depth of our sensors.

It should be emphasized that the results in Fig. 11 demonstrate real imaging acceleration for the 2D water phantom. The SENSE images with $R=2$ and $R=3$ were acquired in 3 min and 2 min, respectively, while single-shot acquisition of the fully encoded image ($R=1$) took 6 min. The SENSE reconstruction, illustrated in Fig. 11, can be successfully applied to both human hand and sheep brain images, reported in this paper. However, imaging these objects with our present system requires signal averaging, so no actual imaging acceleration can be demonstrated for them at this time.

4. Conclusion

In this work, we used our seven-channel SQUID system for 3D ULF MRI and MEG to experimentally demonstrate and study parallel imaging at ultra-low fields. We showed that image acquisition with the sensor array instead of a single sensor substantially improves imaging FOV and SNR. Moreover, 3-fold

imaging acceleration based on the SENSE method was demonstrated at ULF for the first time. These results indicate that parallel imaging techniques are efficient in ULF MRI, and can significantly enhance performance of multi-channel SQUID instruments. As in high-field MRI, accelerated image acquisition is the most promising application of sensor arrays at ULF. The intrinsic SNR of our present system, however, is not high enough to allow accelerated imaging *in vivo*. Thus, the SNR improvement by the sensor array, demonstrated in this paper, remains the main advantage of multi-channel ULF MRI. By using stronger pre-polarizing fields, we should be able to increase the system SNR sufficiently to achieve imaging acceleration in human subject experiments.

Acknowledgments

We gratefully acknowledge the support of the U.S. National Institutes of Health Grant R01-EB006456 and of the Los Alamos National Security, LLC, for the National Nuclear Security Administration of the U.S. Department of Energy Grant LDRD-20060312ER.

References

- [1] J.S. Hyde, A. Jesmanowicz, W. Froncisz, J.B. Kneeland, T.M. Grist, N.F. Campagna, Parallel image acquisition from noninteracting local coils, *J. Magn. Reson.* 70 (1986) 512-517.
- [2] P.B. Roemer, W.A. Edelstein, C.E. Hayes, S.P. Souza, O.M. Mueller, The NMR phased array, *Magn. Reson. Med.* 16 (1990), 192-225.
- [3] L.L. Wald, L. Carvajal, S.E. Moyher, S.J. Nelson, P.E. Grant, A.J. Barkovich, D.B. Vigneron, Phased array detectors and an automated intensity-correction algorithm for high-resolution MR imaging of the human brain, *Magn. Reson. Med.* 34 (1995) 433-439.
- [4] S.M. Wright, L.L. Wald, Theory and application of array coils in MR spectroscopy, *NMR Biomed.* 10 (1997) 394-410.
- [5] D.K. Sodickson, W.J. Manning, Simultaneous acquisition of spatial harmonics (SMASH): fast imaging with radiofrequency coil arrays, *Magn. Reson. Med.* 38 (1997) 591-603.
- [6] K.P. Pruessmann, M. Weiger, M.B. Scheidegger, P. Boesiger, SENSE: sensitivity encoding for fast MRI, *Magn. Reson. Med.* 42 (1999) 952-962.
- [7] K.P. Pruessmann, M. Weiger, P. Bornert, P. Boesiger, Advances in sensitivity encoding with arbitrary k -space trajectories, *Magn. Reson. Med.* 46 (2001) 638-651.
- [8] D.K. Sodickson, C.A. McKenzie, A generalized approach to parallel magnetic resonance imaging, *Med. Phys.* 28 (2001) 1629-1643.
- [9] K.P. Pruessmann, Encoding and reconstruction in parallel MRI, *NMR Biomed.* 19 (2006) 288-299.
- [10] T. Niendorf, D.K. Sodickson, Parallel imaging in cardiovascular MRI: methods and applications, *NMR Biomed.* 19 (2006) 325-341.
- [11] Y. Zhu, C.J. Hardy, D.K. Sodickson, R.O. Giaquinto, C.L. Dumoulin, G. Kenwood, T. Niendorf, H. Lejay, C.A. McKenzie, M.A. Ohliger, N.M. Rofsky, Highly parallel volumetric imaging with a 32-element RF coil array, *Magn. Reson. Med.* 52 (2004) 869-877.
- [12] J.A. de Zwart, P. van Gelderen, X. Golay, V.N. Ikonomidou, J.H. Duyn, Accelerated parallel imaging for functional imaging of the human brain, *NMR Biomed.* 19 (2006) 342-351.
- [13] F.H. Lin, L.L. Wald, S.P. Ahlfors, M.S. Hämäläinen, K.K.

Kwong, J.W. Belliveau, Dynamic magnetic resonance inverse imaging of human brain function, *Magn. Reson. Med.* 56 (2006) 787-802.

[14] M. Hämäläinen, R. Hari, R. Ilmoniemi, J. Knuutila, O. Lounasmaa, Magnetoencephalography – theory, instrumentation, and application to non-invasive studies of the working human brain, *Rev. Mod. Phys.* 65 (1993) 413-497.

[15] R. McDermott, A.H. Trabesinger, M. Möck, E.L. Hahn, A. Pines, J. Clarke, Liquid-state NMR and scalar couplings in microtesla magnetic fields, *Science* 295 (2002) 2247-2249.

[16] R. McDermott, S.K. Lee, B. ten Haken, A.H. Trabesinger, A. Pines, J. Clarke, Microtesla MRI with a superconducting quantum interference device, *Proc. Nat. Acad. Sci.* 101 (2004) 7857-7861.

[17] R. McDermott, N. Kelso, S.K. Lee, M. Möble, M. Möck, W. Myers, B. ten Haken, H.C. Seton, A.H. Trabesinger, A. Pines, J. Clarke, SQUID-detected magnetic resonance imaging in microtesla magnetic fields, *J. Low Temp. Phys.* 135 (2004) 793-821.

[18] M. Möble, W.R. Myers, S.K. Lee, N. Kelso, M. Hatridge, A. Pines, J. Clarke, SQUID-detected *in vivo* MRI at microtesla magnetic fields, *IEEE Trans. Appl. Supercond.* 15 (2005) 757-760.

[19] A.N. Matlachov, P.L. Volegov, M.A. Espy, J.S. George, R.H. Kraus, Jr., SQUID detected NMR in microtesla magnetic fields, *J. Magn. Reson.* 170 (2004) 1-7.

[20] P. Volegov, A.N. Matlachov, M.A. Espy, J.S. George, R.H. Kraus, Jr., Simultaneous magnetoencephalography and SQUID detected nuclear MR in microtesla magnetic fields, *Magn. Reson. Med.* 52 (2004) 467-470.

[21] M.A. Espy, A.N. Matlachov, P.L. Volegov, J.C. Mosher, R.H. Kraus, Jr., SQUID-based simultaneous detection of NMR and biomagnetic signals at ultra-low magnetic fields, *IEEE Trans. Appl. Supercond.* 15 (2005) 635-639.

[22] V.S. Zotev, A.N. Matlachov, P.L. Volegov, H.J. Sandin, M.A. Espy, J.C. Mosher, A.V. Urbaitis, S.G. Newman, R.H. Kraus, Jr., Multi-channel SQUID system for MEG and ultra-low-field MRI, *IEEE Trans. Appl. Supercond.* 17 (2007) 839-842.

[23] M. Burghoff, S. Hartwig, L. Trahms, Nuclear magnetic resonance in the nanotesla range, *Appl. Phys. Lett.* 87 (2005) 054103.

[24] M. Burghoff, S. Hartwig, W. Kilian, A. Vorwerk, L. Trahms, Thiel F, Hartwig S, Trahms L, SQUID systems adapted to record nuclear magnetism in low magnetic fields, *IEEE Trans. Appl. Supercond.* 17 (2007) 846-849.

[25] S.K. Lee, M. Möble, W. Myers, N. Kelso, A.H. Trabesinger, A. Pines, J. Clarke, SQUID-detected MRI at 132 μ T with T_1 -weighted contrast established at 10 μ T-300mT, *Magn. Reson. Med.* 53 (2005) 9-14.

[26] M. Möble, S.I. Han, W.R. Myers, S.K. Lee, N. Kelso, M. Hatridge, A. Pines, J. Clarke, SQUID-detected microtesla MRI in the presence of metal, *J. Magn. Reson.* 179 (2006) 146-151.

[27] A. Macovski, S. Conolly, Novel approaches to low cost MRI, *Magn. Reson. Med.* 30 (1993) 221-230.

[28] N.Q. Fan, M.B. Heaney, J. Clarke, D. Newitt, L.L. Wald, E.L. Hahn, A. Bielecki, A. Pines, Nuclear magnetic resonance with dc SQUID preamplifiers, *IEEE Trans. Magn.* 25 (1989) 1193-1199.

[29] H.C. Seton, J.M.S. Hutchison, D.M. Bussel, A 4.2K receiver coil and SQUID amplifier used to improve the SNR of low-field magnetic resonance images of the human arm, *Meas. Sci. Technol.* 8 (1997) 198-207.

[30] K. Schlega, R. McDermott, J. Clarke, R.E. de Souza, A. Wong-Foy, A. Pines, Low-field magnetic resonance imaging with a high- T_c dc superconducting quantum interference device, *Appl. Phys. Lett.* 75 (1999) 3695-3697.

[31] Ya.S. Greenberg, Application of superconducting quantum interference devices to nuclear magnetic resonance, *Rev. Mod. Phys.* 70 (1998) 175-222.

[32] J. Stepišnik, V. Eržen, M. Kos, NMR imaging in the Earth's magnetic field, *Magn. Reson. Med.* 15 (1990) 386-391.

[33] A. Mohorič, G. Planinščič, M. Kos, A. Duh, J. Stepišnik, Magnetic resonance imaging system based on Earth's magnetic field, *Instrum. Sci. Technol.* 32 (2004) 655-667.

[34] G. Stroink, W. Moshage, S. Achenbach, Cardiomagnetism, in: W. Andrä, H. Nowak (Eds.), *Magnetism in Medicine*, Wiley-VCH, Berlin, 1998, pp.136-189.

[35] P.L. Volegov, J.C. Mosher, M.A. Espy, R.H. Kraus, Jr., On concomitant gradients in low-field MRI, *J. Magn. Reson.* 175 (2005) 103-113.

[36] W.R. Myers, M. Möble, J. Clarke, Correction of concomitant gradient artifacts in experimental microtesla MRI, *J. Magn. Reson.* 177 (2005) 274-284.

[37] D.A. Yablonskiy, A.L. Sukstanskii, J.J.H. Ackerman, Image artifacts in very low magnetic field MRI: the role of concomitant gradients, *J. Magn. Reson.* 174 (2005) 279-286.

[38] M.A. Ohliger, D.K. Sodickson, An introduction to coil array design for parallel MRI, *NMR Biomed.* 19 (2006) 300-315.

[39] M. Weiger, K.P. Pruessmann, P. Boesiger, 2D SENSE for faster 3D MRI, *MAGMA* 14 (2001) 10-19.